

Contents lists available at ScienceDirect

# Spectrochimica Acta Part B: Atomic Spectroscopy

journal homepage: www.elsevier.com/locate/sab





# A demonstration of spatial heterodyne spectrometers for remote LIBS, Raman spectroscopy, and 1D imaging $^{\Rightarrow}$

K. Alicia Strange Fessler<sup>a</sup>, Abigail Waldron<sup>b</sup>, Arelis Colón<sup>b</sup>, J. Chance Carter<sup>c</sup>, S. Michael Angel<sup>b</sup>,<sup>a</sup>

- <sup>a</sup> Savannah River National Laboratory, Bldg. 999-2W, Room CO2, Aiken, SC 29808, USA
- b University of South Carolina, Department of Chemistry and Biochemistry, 631 Sumter Street, Columbia, SC 29208, USA
- <sup>c</sup> Lawrence Livermore National Laboratory, Materials Science Division, 7000 East Ave., Livermore, CA 94550-5507, USA

#### ARTICLE INFO

# Keywords: Remote Raman Remote LIBS Monolithic Raman spectrometer Spatial heterodyne spectrometer Spatial heterodyne Raman spectrometer Raman LIBS

#### ABSTRACT

Three spatial heterodyne Raman spectrometers, one free standing, the others monolithic, have been used for remote Raman and IIBS for samples at a distance of 4.5 m and 1D Raman imaging. The wide area measurement capability of the SHS was demonstrated and shown to reduce sample photodegradation in the case of Raman, using large laser spots on the sample, without loss of signal or decreased spectral resolution. 1D Raman imaging using a free standing SHRS and a monolithic SHRS was demonstrated and shown to provide better signal-to-noise ratio (SNR) spectra for heterogenous samples than spectra measured without imaging. Improved SNR using 1D imaging is the result of spatial separation of the signal from different areas of the sample, which reduces the contribution of shot noise from stronger scattering sample regions to more weakly scattering adjacent sample regions. For 1D imaging of adjacent samples, within the field-of-view (FOV) of the spectrometer, the SNR improved up to four times, with no loss of spectral resolution or spectral range, and a spatial resolution of 280 µm was demonstrated for samples located at 4.5 m from the spectrometer.

## 1. Introduction

Active remote spectroscopic analysis can be performed by using a laser to excite a sample at distances of tens to hundreds of meters, while using a small telescope to collect scattered light in the case of Raman, or emitted light in the case of luminescence and LIBS, and directing the collected light into a spectrometer. Remote atomic analysis using LIBS was described as early as 1995 [1], and many early papers describe remote LIBS for explosives detection [2–5]. In the case of remote LIBS, the useful range is limited to 10s of meters by the ability to produce a remote spark on the sample. Molecular analysis using remote Raman spectroscopy was first described and demonstrated for atmospheric gas measurements [6–9], and was later extended to measurements of inorganic and organic compounds using a portable remote Raman system developed for radioactive wastes analysis in underground storage tanks [10], and this is still the basis for this technique. Although Raman scattering is a weak process, the quality of the laser spot on a remote

sample is not as important as in LIBS, and remote Raman at distances up to 1500 m has been demonstrated [11]. Raman and LIBS provide complementary information (e.g., molecular and atomic) and the spectrometers used to make remote Raman and LIBS measurements share many common elements, such as a laser, a large collection optic, a gated detector, and a wavelength analyzer. Therefore, it is logical to combine the two spectroscopies in a common instrument. A combined remote Raman/LIBS instrument was first described by Sharma, et al., in 2007 [12], and since then several such instruments have been described for minerals analysis and for explosives detection [5,12–15]. An instrument that combines Raman and LIBS, called SuperCam, is included on the Mars2020 perseverance Royer [16].

All of the instruments described above for remote Raman and LIBS use conventional, dispersive monochromators for spectral analysis. In 2011, Gomer et al. demonstrated the use of a fixed grating interferometer, the spatial heterodyne spectrometer (SHS) for Raman spectroscopy (SHRS) [17], and this work was later extended by Lamsal, et al. to deep

E-mail address: smangel0@mailbox.sc.edu (S.M. Angel).

<sup>\*</sup> This article is published in a special honor issue dedicated to Richard E. Russo to commemorate his 70th. birthday, for his achievements in the fields of laser-material interaction, plasma modeling and evolution, surface analysis with lasers, and for his vision of what is needed and critical in future theoretical, instrumental and methodological development.

<sup>\*</sup> Corresponding author.

UV [18,19] and remote UV Raman measurements [19,20], and it has since been demonstrated for remote Raman and LIBS. An SHS based LIBS spectrometer was first described by Gornushkin, et al. [21] and was later extended by Barnett, et al. to remote LIBS [22]. Although using a SHS for Raman and LIBS does not provide a signal-to-noise advantage for most common Raman or LIBS measurements, the wide field of view and correspondingly high throughput can be an advantage for applications where light is collected from an extended source, such as in transmission Raman [23]. The system design lends itself to miniaturization and the use of monolithic construction techniques, which can be an advantage when spectrometer size and robustness are important, such as might be needed for in spacecraft or planetary rovers. Our group recently demonstrated the first monolithic SHS used for Raman spectroscopy, designed for use in planetary spacecraft [24].

The SHS is a fixed grating interferometer with no moving parts so all wavelengths are measured simultaneously, which makes the system compatible with the pulsed lasers and gated detection that are most often used for remote spectroscopy. The SHS does not require an entrance slit to maintain high resolution and has a large angular field-ofview (FOV), making the optical etendue of the system larger than that of a conventional dispersive spectrometer. The large etendue of the SHS allows wide area measurements to be made without losing sensitivity or spectral resolution, and sample photodegradation can be avoided by using large laser spots on the sample. For remote Raman and LIBS measurements, the large entrance aperture of the SHS can reduce telescope alignment constraints and minimize laser pointing stability issues, because small movements of the laser spot on the target, or movement of the LIBS plasma, do not reduce the amount of light collected by the spectrometer, as recently demonstrated in our laboratory using a bench top SHS for remote LIBS measurements [22]. In this paper three different SHS spectrometers for remote Raman, LIBS and 1D imaging were demonstrated for samples at a distance of 4.5 m. Two of the spectrometers used in this work are constructed using monolithic techniques and represent the first use of a monolithic SHS for remote LIBS and 1D imaging.

# 2. Experimental

## 2.1. Spatial heterodyne raman spectrometers

## 2.1.1. Free standing SHS

Three SHS systems were used for this work, a benchtop free-standing

SHS (FS SHS) for remote Raman and 1D Raman imaging, and two different monolithic SHS (mSHS) spectrometers, used for remote LIBS and Raman 1D imaging. Fig. 1 shows a schematic of the SHRS. The basic instrument design was previously described [17–40]. The SHRS benchtop system consisted of a 25 mm cube beam splitter (CM1-BS013, ThorLabs) and two 25 mm, 150 grooves/mm diffraction gratings blazed at 500 nm. A grating mount (DGM-1; Newport Corp.) was used to manually control the grating rotation angle to precisely set the Littrow wavelength. A 105 mm focal length, f/2.8 lens (AF Micro-Nikkor; Nikon) was used to image the gratings at unity magnification onto a liquid nitrogen cooled charge-coupled device (CCD) detector with 1340  $\times$  1300, 20  $\mu$ m pixels (VersArray; Princeton Instruments). The fringe pattern was recorded on the CCD using Winspec (32-bit, version 2.5.22.0), and data processing was performed using Matlab (MathWorks, version R2013a) and IGOR Pro (WaveMetrics, version 6.03A2) software.

A 532 nm diode-pumped continuous wave (CW) laser (Millennia Pro 2 s; Spectra-Physics) was used as the excitation source for all spectra presented and to set the Littrow angle of the gratings to 532 nm. For remote Raman, light was collected and collimated from the remote sample using a 60 mm diameter, 490 mm focal length achromatic lens (L1), and focused through a spatial filter, collimated to a 25 mm diameter beam using an achromatic, 250 mm focal length, 50.8 mm diameter, MgF2 coated lens, L2, (PAC088; Newport Corp.) and directed into the SHRS. For 1D imaging, L2 was replaced by a 200 mm focal length, 25.4 mm diameter achromatic lens, and an additional 400 mm focal length. 30 mm high planoconvex cylindrical lens was placed in the collimated input beam. The collimated light was filtered using various combinations of three filters: a 600 nm short-pass filter (10SWF-600-B; Newport Corp.) to block out-of-band light, and a 532 nm long-pass filter (LP03-532RE-25; Semrock) and 532 nm holographic filter (Supernotch; Kaiser Optical Systems Inc.) for laser line rejection. Filters limited the aperture to 22.8 mm.

# 2.1.2. Monolithic SHS

Two monolithic spatial heterodyne spectrometers used for Raman imaging (mSHRS) and remote LIBS (mSHLS) measurements were custom built by LightMachinery, Inc. (Ottawa, ON K2E 7 L2 Canada), one is shown as a picture inset in Fig. 1. The mSHS spectrometers consisted of two 15 mm by 15 mm diffraction gratings, a 25 mm N-BK7 50:50 cube beam splitter, and two N-BK7 spacers that define the angle the gratings are tilted in the horizontal plane (e.g., the dispersion plane) with respect to the optical axis. All optical faces were antireflection

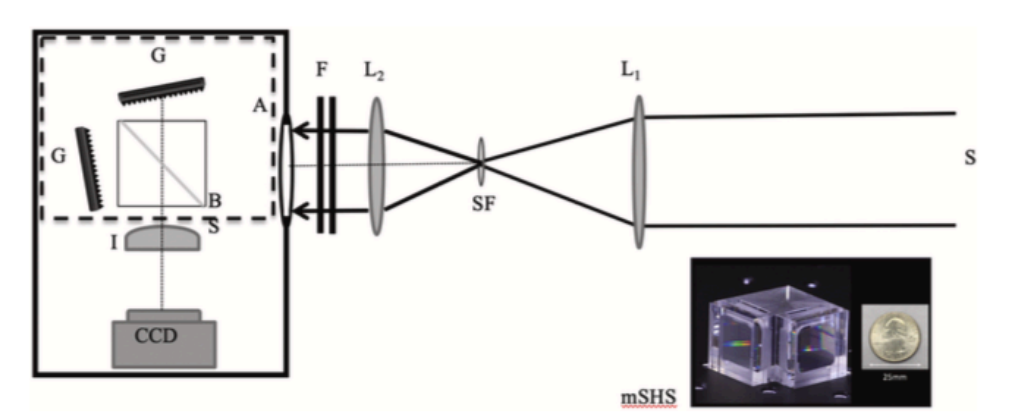


Fig. 1. Benchtop SHRS schematic: Light from the sample is collected by lens L<sub>1</sub>, focused through a spatial filter SF, collimated by lens L<sub>2</sub> and directed into the SHS entrance aperture (A). The light is split by a 50/50 beamsplitter (B), and directed to gratings (G) which reflect and disperse the beams which recombine at the beamsplitter, and form an interference pattern of vertical fringes which are imaged onto the detector by imaging lens I.

mSHS: monolithic spatial heterodyne spectrometer with 150 gr/mm gratings, compared in size to a US Quarter. It takes the place of the optics inside the dashed line box to the left.

coated to minimize spurious reflections from the 0th and 2nd order diffracted beams, and all components are epoxied to make a single optical component. Both mSHS devices used 150 grooves/mm gratings. The mSHS used for Raman 1D imaging had a 616.8 nm Littrow wavelength, while the monolith used for remote LIBS had a 531.6 nm Littrow wavelength. Both mSHS devices are about  $3.5 \times 3.5 \times 2.5$  cm in size and weigh about 80 g.

For SHS Raman 1D imaging, the mSHRS spectrometer setup is very similar to that shown in Fig. 1, except the monolith SHS was used in place of the free standing SHS, A 532 nm continuous wave Nd: YAG laser (OptoEngine, MGL-FN-532 nm-1 W) was used as the excitation source for all spectra and the laser power on the sample was approximately 165 mW. The laser beam was directed onto the sample using a 50 mm diameter, 550 nm long pass dichroic mirror (ThorLabs, DMLP550L) at 45°. An f/6 laser focusing lens, not shown, was placed before the 45° laser turning mirror and used to create a beam spot 3 mm in diameter on the samples, at S. The samples were contained in two vertically stacked 1 cm quartz cuvettes, shown in the insert picture in Fig. 1. The Raman scattered light was collected by an f/4 lens, L1, focused through a spatial filter and then collimated by another f/4 lens, L2, into the mSHRS through three 14 mm circular apertures placed ~20 cm apart, to ensure beam collimation and to limit the beam size to 14 mm so as not to overfill the mSHRS gratings. A 20 mm tall cylindrical lens with a focal length of 250 mm was placed on the collection axis, between the filters and the input aperture, 250 mm from the gratings, to form an image of the sample in the vertical plane on the grating face of the mSHS. The cylindrical lens was removed for spectra taken in a non-imaging mode.

Two filters, F, a 532 nm long pass filter (Semrock RazorEdge, LP03-532RE-25) and a 532 nm holographic notch filter (Supernotch, Kaiser Optical Systems, Inc.) were placed in front of the mSHRS to remove strong laser scatter. An additional short pass filter was used to limit the total spectral range (bandpass) allowed into the spectrometer, a 581 nm short pass filter (Knight Optical, 581FDS25). A CCD detector with 1340  $\times$  400, 20  $\mu m$  pixels (Princeton Instruments, PIXIS 400) cooled to  $-70\,^{\circ}\text{C}$ , was used for all measurements. A fused silica 105 mm focal length, f/4.5 camera lens, I, (Coastal Optical Systems, Inc., UV-MICRO-APO 111032) was used to image the grating faces onto the CCD detector at a magnification of  $-1.6\times$  to fill as much of the detector in the horizontal direction as possible. For all measurements, a spatial filter was placed one focal length behind the imaging camera lens, on the CCD side, to block higher grating diffraction orders.

For mSHS LIBS measurements, a plasma was generated on the sample using a Continuum Surelite III (Continuum, San Jose, CA, USA) pulsed laser, doubled to 532 nm at ~87 mJ/pulse for benchtop measurements and ~200 mJ/pulse for all remote measurements. The laser was focused onto the sample off-axis, using an f/2 silica lens for benchtop measurements. In the case of remote LIBS measurements, samples were excited off axis using either a 5× beam expander or an f/4 lens to control the spot size on the sample. A Nikon AF Nikkor 85 mm f/4 1:1.8D lens (Nikon, Tokyo, Japan) was used to image the plane of the monolithic SHS diffraction gratings onto a thermoelectrically cooled 1024 × 256 pixel, gated ICCD array detector with 26 µm pixels (Princeton Instruments, Model PIMAX4). The imaging lens was set up to provide a ~1.7 times magnification so the image of the 14 mm diffraction grating on the detector was ~24 mm, almost filling the detector in the horizontal direction but overfilling the vertical direction.

# 2.2. Samples

Sulfur, potassium perchlorate, sodium nitrate, sodium nitrite, sodium sulfate, and ammonium nitrate were purchased from Sigma-Aldrich at 99 + % purity and used "as is." Calcite, α-quartz, gypsum, and olivine were natural rock and mineral samples. Copper plates obtained from an industrial supply company of unknown purity, magnesium rods (99.9 + %, Sigma-Aldrich), manganese chips (99%, Sigma-Aldrich) and iron filings of unknown purity pressed into a pellet were

used for LIBS measurements.

#### 3. Results and discussion

#### 3.1. Spatial heterodyne spectrometer

The basic design and operation of the SHRS has been discussed previously [17–40]. In the interferometer, collimated light is passed through a 50/50 beam splitter, dividing the beam into two parts which are directed onto tilted diffraction gratings. After being diffracted off the gratings, the beams recombine at the beamsplitter as crossing wave fronts. The gratings are tilted at an angle,  $\theta_L$ , such that a particular wavelength, the Littrow wavelength,  $\lambda_L$  is retro-reflected and recombined so no interference pattern is produced. For any wavelength other than Littrow, the crossed wave fronts will generate a fringe pattern, which is imaged onto the CCD to produce a fringe image. By taking a Fourier transform of the fringe image, an intensity spectrum can be obtained. The intensity of the fringe pattern as a function of position x on the detector is given by Eq. (1),

$$I(x) = \int_{0}^{\infty} B(\sigma) \{1 + \cos[8\pi(\sigma - \sigma_L)x \tan\theta_L]\} d\sigma \qquad (1)$$

Where  $B(\sigma)$  is the input spectral intensity at wavenumber  $\sigma$ , x is the position on the detector, and the other variables are defined above. The Fourier transform of I(x) yields the Raman spectrum. The fringe frequency on the detector is given by Eq. (2),

$$f = 4(\sigma - \sigma_L)tan\theta_L$$
 (2)

where f is fringes per centimeter,  $\sigma$  is the wavenumber of the Raman band of interest,  $\sigma_L$  is the Littrow wavenumber, and  $\theta_L$  is the Littrow angle. Due to the symmetry in Eq. (2), spectral bands above or below the Littrow wavelength show identical fringe patterns, leading to degenerate bands, or band overlap. By tilting one grating vertically, and thus rotating the fringes, this overlap can be removed, and this allows doubling of the useful wavelength range [17].

Unlike dispersive spectrometers, the SHS does not require a slit to control the spectral resolution and the spectral resolution is not a function of the focal length of the device. Instead, the resolving power of the SHS is proportional to the total number of grooves illuminated on both gratings. For a SHS built with two fully illuminated gratings of size W and groove density d, the resolving power is expressed as Eq. (3): about 6800 for the benchtop free standing SHS and 4200 for the mSHS, giving 2.6 cm<sup>-1</sup> and 4.4 cm<sup>-1</sup> (0.12 nm at 532 nm) theoretical spectral resolution, respectively. In practice the resolution is usually lower, limited by the number and size of detector pixels illuminated, and imperfect optics. The spectral resolution of the benchtop free standing SHRS was measured using a low-pressure Hg lamp to be ~8 cm<sup>-1</sup>. Factors that can affect the SHS resolution include camera focusing collimation of the input beam, the size and number of detector pixels illuminated, and the quality of the gratings and imaging optics.

$$R = 2Wd$$
 (3)

The collection solid angle is related to the resolving power by Eq. (4). The full acceptance angle for the 150 gr/mm SHRS is about  $2^\circ$ , or  $1^\circ$  for the half angle. Due to both the large entrance aperture,  $\sim 15$  mm for the SHRS, and large collection solid angle, the SHRS has a higher throughput than a conventional dispersive spectrometer. This higher throughput of the SHS does not necessarily translate into higher sensitivity, but for collecting light from large extended sources, the SHS can give a signal advantage.

$$\Omega = \frac{2\pi}{R}$$
(4)

For the free standing SHRS system used here, the collection solid angle is about 9.2  $\times$  10 $^{-4}$  sr, giving an acceptance angle of  $-3\times10^{-2}$ 

rad (i.e.  $1.7^\circ$ ). The calculated width of the area viewed with the optical set up described here, for a sample distance of 4.5 m is -66 mm. For the mSHLS spectrometer the maximum, resolution-limited solid angle field of view (FOV) was  $1.4\times10^{-3}$  sr, with a full acceptance angle of about  $1.3^\circ$ .

#### 3.2. Representative spectra

Fig. 2 shows Raman spectra of some common minerals, calcite,  $\alpha$ -quartz, olivine, and gypsum, which are of interest for Mars exploration [41]. These spectra were measured using the benchtop free standing SHRS with a 60 mm collection lens, with the samples at a distance of 4.5 m. The measured spectral resolution for the sample Raman bands ranged from ~11 to ~13 cm<sup>-1</sup>. The measured spectra match well to Raman spectra reported for similar samples in the literature. The symmetric breathing vibration of carbonate at 1086 cm<sup>-1</sup> is the most prominent Raman band in the calcite spectrum [42]. The Raman spectrum of quartz displays the silica symmetric vibrational modes at 210, 357, and 468 cm<sup>-1</sup> which are characteristic of low temperature phase α-quartz [43]. Olivine is a silicate-based mineral, and the silicate Raman bands present in the spectrum are the stretching combinations at 821 and 854 cm<sup>-1</sup>, and the anti-symmetric stretches at 919 and 960 cm<sup>-1</sup> [44]. The gypsum (CaSO<sub>4</sub> · 2H<sub>2</sub>O) Raman spectrum has six characteristic Raman bands of the sulfate ion: the symmetric stretch at 1008 cm<sup>-1</sup>, anti-symmetric bending at 412 and 495 cm<sup>-1</sup>, anti-symmetric stretch at 1135 cm<sup>-1</sup> and anti-symmetric bending at 613 and 672  $\mbox{cm}^{-1}$  [45].

All four samples show some degree of luminescence, and no attempt was made to remove the luminescence from the spectra shown in Fig. 2. The interferogram for each sample, taken by summing the intensity of vertical fringes in the fringe image, is shown as an inset in Fig. 2. The quality of the interferogram is given by the fringe visibility (FV), which is defined by Eq. (5). The FV was relatively high, at 0.11, 0.17, 0.26, and 0.23 for the calcite,  $\alpha$ -quartz, olivine, and gypsum samples, respectively.

$$FV = (I_{max} - I_{min})/(I_{max} + I_{min})$$
(5)

Width of area viewed and off-axis detection at  $4.5\ m$  with free standing SHRS.

The large acceptance angle of the SHRS allows for wide area

measurements to be made without losing sensitivity or spectral resolution, unlike a slit-based dispersive spectrometer that requires all light to enter through a narrow slit to maintain high spectral resolution. Although measurements with large laser beam diameters have been demonstrated using an SHRS [17,19,20], the laser spot sizes were never close to limit of the width of area viewed by the SHRS. Therefore, measurements were made using laser spots up to 50 mm diameter to test the limits of the viewable area. The  $\sim\!\!1^\circ$  acceptance angle of the SHS provides about a 66 mm diameter field of view at 4.5 m but adding the 60 mm collection lens decreases the field of view significantly.

The large field of view makes the SHS uniquely suited for remote spectroscopy and remote 1D imaging. Fig. 3a demonstrates the width of the area viewed as a plot of the Raman intensity for a sulfur sample located at 4.5 m distance versus the size of the laser spot at the sample from -200 um to -50 mm. The inset shows all 16 Raman spectra overlapped for each beam size measured, and the intensity did not change appreciably as the laser spot size varied while the resolution was constant. The size of the laser spot on the sample was measured using a razor edge to block the beam as the power was measured. The diameter of the laser spot at the sample was taken as the distance between the 5% and 95% values in the plot of intensity versus laser spot diameter. The plot shows a slight decrease in intensity at the largest laser spot sizes, but up to -50 mm there is no significant loss of the Raman signal.

In Raman, lower laser flux can be used to decrease laser induced degradation of the sample, and the large field of view can be used to advantage in this respect [17–20]. Fig. 3b shows the 219 cm<sup>-1</sup> sulfur Raman band intensity as a function of laser power for different laser spot sizes, and thus different sample irradiance. The laser irradiance on the sample for the 0.25, 3, 19, and 64 mm laser spots was varied by a factor of ten, between 240 and 2400, 1.7–17, 0.043–0.42, and 0.0037–0.037 W/cm<sup>2</sup>, respectively. The sample was moved between each measurement for the 0.25 mm and 3 mm beams. At the larger beam sizes, the Raman intensity increases in proportion to the laser power increase, as expected if there is no sample degradation. However, the smaller spot size, higher laser irradiance, curves are nonlinear indicating sample degradation. These results show no sample degradation when the laser irradiance at the sample was below -0.42 W/cm<sup>2</sup>, corresponding to a spot size of 19 mm or greater. Significant sample degradation (sample

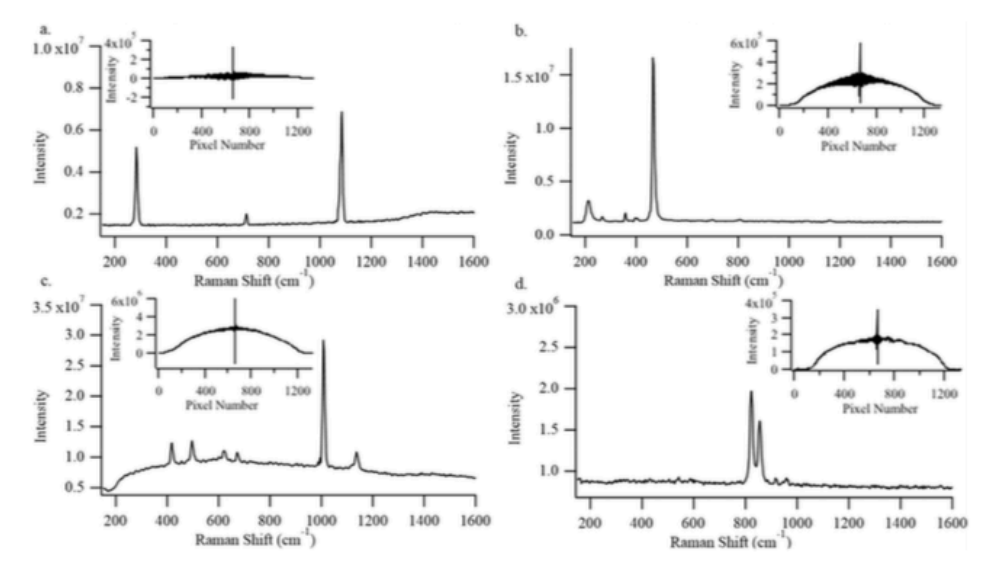


Fig. 2. Raman spectra and corresponding fringe cross sections of mineral samples at 4.5 m distance, measured with the benchtop SHRS using a 2 W, 532 nm laser. The top two spectra, calcite (a.) and quartz (b.), were measured using a 30 s acquisition. The lower two spectra, gypsum (c.) and olivine (d.), were measured using 60 s and 90 s acquisitions, respectively.

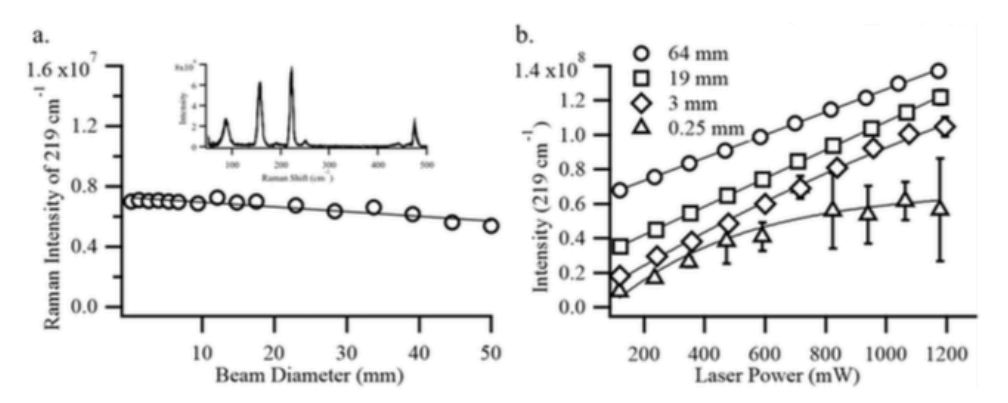


Fig. 3. a. Plot of Raman intensity of the  $219 \, \mathrm{cm}^{-1}$  sulfur band, as laser spot size at the sample is increased from  $\sim 200 \, \mu \mathrm{m}$  to  $\sim 50 \, \mathrm{mm}$ , at constant laser power,  $200 \, \mathrm{mW}$ , using a  $10 \, \mathrm{s}$  acquisition. Inset: Sulfur Raman spectra for each laser spot size.

b. Plot of the Raman intensity of the  $219 \, \mathrm{cm}^{-1}$  sulfur band as laser power is varied for different laser spot sizes, indicated inset, on the sample. Curves offset for clarity.

was visibly burned in some instances) was observed for the 0.25 mm spot size at laser powers greater than 400 mW and attributed to the large error measured for the higher irradiated spots.

Fig. 4 shows the Raman intensity of KClO<sub>4</sub> and Na<sub>2</sub>SO<sub>4</sub> as the laser spot is moved off the optical axis of the spectrometer for the samples at a distance of 4.5 m. The sample and laser were positioned on the optical axis and the laser spot moved in small increments in the horizontal direction. Note: During the off-axis experiments using the Na2SO4 sample, a 9 mm aperture was used as a spatial filter, see Fig. 1. The Raman spectra of the Na<sub>2</sub>SO<sub>4</sub> and KClO<sub>4</sub> samples are inset in Fig. 4. The distance at which the Raman intensity drops to 1/e of the maximum intensity for the Na2SO4 and KClO4 samples is ~37 and 40 mm, respectively, from the optical axis, which corresponds to a ~74-80 mm full width field of view, and an angular FOV of ~1.8-2°, consistent with the theoretical value for the benchtop SHS. The slight intensity increase around 1 cm in Fig. 7 is consistent with results reported using spatially resolved spectroscopy for highly scattering samples as described by Oelkrug, et al. [46-47] Diffuse scattering can lead to stronger Raman signals originating from a sample region slightly shifted from the point where the sample is illuminated by the laser [46,48].

The monolithic SHS (mSHS) described here for LIBS and Raman

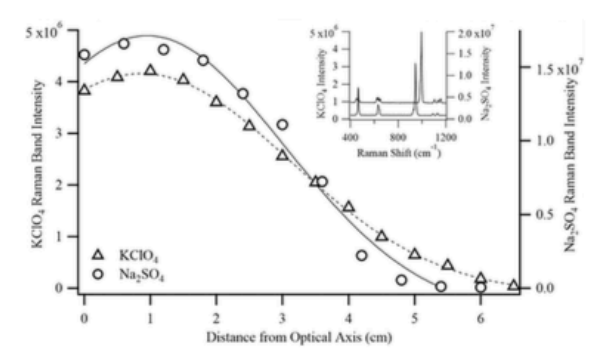


Fig. 4. Plot of the Raman intensity of potassium perchlorate (triangles, left axis) and sodium sulfate (circles, right axis) as the laser spot on the sample is moved away from optical axis. Inset: Raman spectra of potassium perchlorate (lower) and sodium sulfate (top), offset for clarity. KClO<sub>4</sub> was contained in a 1 cm cuvette, and was measured using ~700 mW with 15 s acquisitions. Na<sub>2</sub>SO<sub>4</sub> was measured as a 10 cm diameter pellet, measured using ~1.5 W with 30 s acquisitions.

measurements is very small,  $3.5 \times 3.5 \times 2.5$  cm, but provides a spectral resolution that is comparable to a high performance, in most cases much larger, dispersive monochromator, and the mSHS has much higher light throughput. The etendue of the mSHS used here is  $2.5 \times 10^{-3}$  sr•cm², calculated using the  $1.4 \times 10^{-3}$  sr collection solid angle and 15 mm aperture. As a rough comparison, an f/4 dispersive monochromator of comparable spectral resolution using a  $10~\mu m$  input slit, would have an etendue of  $4.9 \times 10^{-5}$  sr•cm²,  $\sim 50$  times lower than the mSHS. This comparison assumes the field of view of the sample in both cases is limited by the width of the input aperture of the spectrometer, and in the case of a slit based aperture, there are ways to use the height of the slit to increase the light throughput.

The high resolution of the mSHS makes it very suitable for LIBS, however the spectral range is limited by the number of detector pixels available. For the CCD detector used for mSHLS measurements, with 1024 horizontal pixels, 512 spectral elements can be resolved. At the theoretical resolution of the mSHS gratings, this should give a spectral range of ~2250 cm<sup>-1</sup>, or ~72 nm, and as much as 144 nm with wavelength doubling using a 2D SHS.

One of the principal weaknesses of the SHS is the way noise from strong signals deteriorates the SNR of weaker signals. This is because in the SHS, as any interferometer, noise is equally distributed across all spectral features. Thus, it is critical for LIBS and Raman measurements with the SHS that filters are used to suppress strong features that are outside the spectral region of interest. For Raman this mostly involves strong Rayleigh scattering from the sample or surrounding regions. In the case of LIBS, strong lines outside the spectral region of interest should be blocked. In a recent paper, Egan et al. demonstrated a cross dispersion SHS that minimizes this problem without the use of filters, increasing the SNR for weak Raman lines over an order of magnitude [53].

Benchtop LIBS spectra using the monolithic SHS of copper and manganese (see Fig. 5a and b), were taken with the samples 1.0 m from the mSHLS entrance aperture. No collection optics were needed, because at this distance, emission light reaching the input aperture was roughly parallel and the emission strength was very high, so light collected just using the mSHS 14 mm gratings provided sufficiently high signal to noise ratio. The laser power was ~87 mJ/pulse for these measurements, with a ~400 µm diameter spot size at the target. Each sample spectrum was acquired using 500 laser shots. Remote LIBS spectra of copper and manganese at 4.5 m are shown in Fig. 5c and d. These elements show relatively strong emission lines in this spectral range with good signal to noise ratio. The FWHM of the strongest emission lines for both elements are about 0.2 nm which is very close the mSHS theoretical resolution.

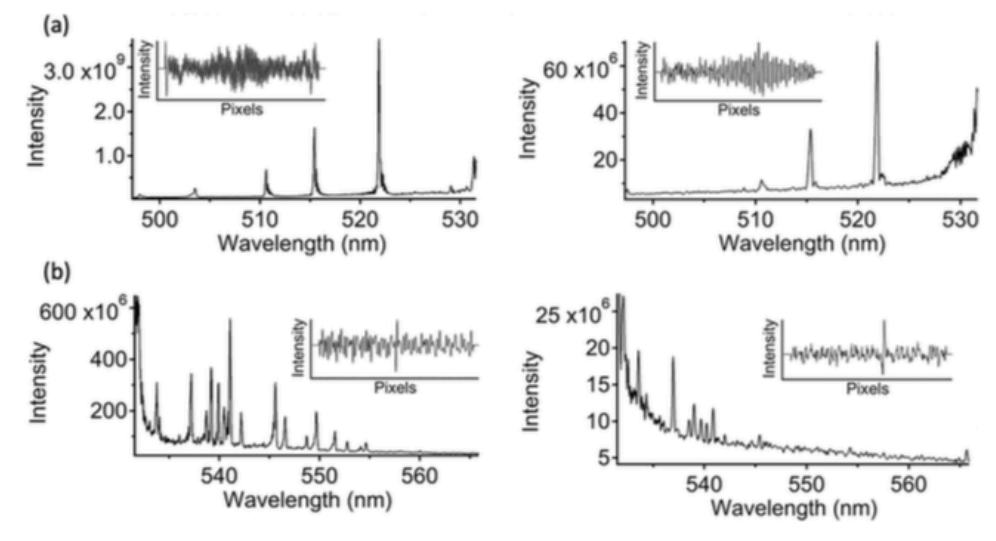


Fig. 5. LIBS spectra of (a) copper metal and (b) manganese metal using the monolithic SHS, for samples at 1 m (e.g., benchtop, left) and remote at 4.5 m (right). Insets: interferogram/cross sections for each spectrum, generated by summing the intensity of each column of pixels in the fringe image and applying background subtraction. The gate delay was  $2.2 \mu s$  and  $0.35 \mu s$  for copper, for benchtop and remote measurements, respectively. Because of software issues, the gate width, rather than gate delay, was changed to compensate for the delay of the emission signal reaching the detector after the laser shot,  $10 \mu s$  and  $2000 \mu s$  for all benchtop and the standoff measurements, respectively. This resulted in higher than expected noise for the remote measurements. Benchtop measurements were made using 500 laser shots while 1000 s shots were used for the remote measurements.

The insets show the interference fringe pattern, background subtracted. The FV was 0.11 for Cu and 0.29 for Mn. The three strong Cu lines at ~510, 515 and 522 nm (note, these are below the mSHS Littrow wavelength) match Cu emission lines listed in the NIST spectral data base [49]. The Cu spectrum was calibrated in wavelength using the known wavelengths of the three strong Cu I lines. This calibration curve was useful in identifying lines in other spectra as well as locating lines at wavelengths above the Littrow wavelength that overlapped the spectral region shown. Two very weak lines, shown at ~496 and 502 nm match Cu I emission lines at 570 and 563 nm, respectively. As shown by Eq. (2), lines like this above the Littrow wavelength also show up below Littrow, unless blocked by appropriate filters. In the case of the Mn emission spectra, a 532 nm long pass filter was used to prevent overlap of lines below the Littrow wavelength. For remote LIBS, the number of laser shots was increased from 500 to 1000 for each measurement, to compensate partly for the reduced signal. The FV for the remote measurements were 0.10 for Cu and 0.26 for Mn, similar to the benchtop measurements.

The theoretical acceptance angle of the mSHLS is ~1.3°, corresponding to a FOV at 4.5 m of ~100 mm. To test the system acceptance angle, the FOV was measured by placing a 110 mm wide strip of Cu, 4.5 m from the front of the spectrometer with the center of the Cu strip aligned with the optical axis of the spectrometer. Spectra were collected in triplicate with the laser focus directed by a 5× beam expander in random order to positions along the Cu strip. Fig. 6 shows the baselinesubtracted intensity of the 522 nm Cu line, plotted as a function of angle from the optical axis. The plot shows the intensity is relatively constant within +/- one degree from the optical axis, then drops off quickly at larger angles. This result agrees well with the expected theoretical acceptance angle of the mSHLS. The rapid decrease in intensity at angles greater than ~0.6° is because the light travels through the SHLS at such an extreme angle that part of the beam completely misses the ICCD. This demonstrated high tolerance to off axis light entering the mSHS, suggesting relaxed tolerance of the mSHLS for remote LIBS measurements from such things as laser pointing stability, and random movement of the plasma image.

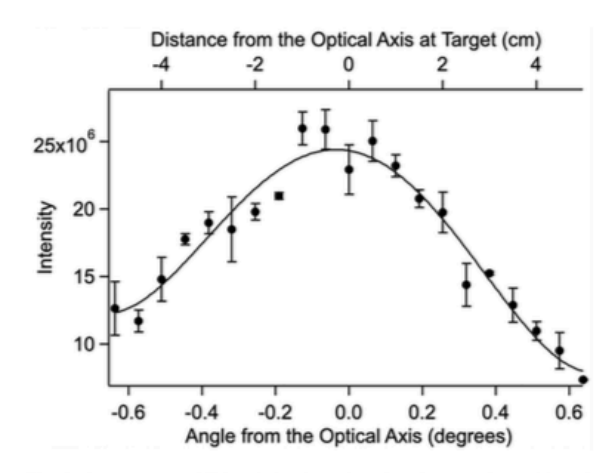


Fig. 6. Copper remote LIBS emission intensity, plotted versus the position of the focused laser spot on the sample, relative to the optical axis, with the copper sample placed 4.5 m from the mSHLS. Each position was repeated in triplicate with the position of the laser spot randomized. No collection optics were used for these measurements, other than the 15 mm mSHS gratings.

# 3.3. 1D imaging using a SHRS

Raman imaging is a powerful technique to analyze heterogeneous or mixed samples. For example, the spatial distribution of the heterogeneities in a geological sample can provide information about how the geological samples were formed [50]. The SHRS is well suited to Raman imaging, and Smith, et al. described several approaches to imaging with the SHS [51]. For 1D SHRS imaging, a cylindrical lens is added to the collection optics to focus an image of the sample onto the gratings in the vertical direction. In the SHRS, the gratings, along with the sample image are imaged onto the CCD. For the imaging studies, the optical set

up is similar to that in Fig. 1, except  $L_2$  was replaced by a 200 mm focal length, 25.4 mm diameter achromatic lens, and a 400 mm focal length, 30 mm high cylindrical lens was placed between the  $L_2$  and the gratings to image the remote sample onto the gratings.

To test 1D Raman imaging with the benchtop SHRS, a mixed sample was constructed by vertically stacking three 1 cm cuvettes containing KClO<sub>4</sub>, NH<sub>4</sub>NO<sub>3</sub>, and a NaNO<sub>3</sub>/NaNO<sub>2</sub> mixture, as shown by the picture inset, Fig. 7a. The samples were illuminated using a 3.5-4.0 cm laser spot. The spatial resolution at this distance, ~280 μm, was determined by imaging wires of known thicknesses, placed at the sample position. Fig. 7 shows Raman spectra, and the corresponding CCD fringe images of the samples with the use of the cylindrical imaging lens (b), and without the cylindrical lens (c). In Fig. 7b the cuvettes are clearly resolved vertically but not horizontally, while there is no spatial resolution in either direction in c. The Raman spectrum measured without the imaging lens (labeled as Collimated) clearly shows all four components with good spectral resolution, but not spatially resolved. The top three Raman spectra show the components of each sample separately, where each spectrum was extracted from the top, middle, and lower portions of the 1D Raman fringe image by vertically grouping the rows corresponding to the three cuvettes. A row-by-row FFT for each cuvette image was used to obtain the Raman spectra. The spectral resolution, ~8 to 13 cm-1, was the same for both imaging and non-imaging measurements because the cylindrical lens does not affect dispersion in the horizontal plane. More importantly, the signal-to-noise ratio (SNR) of the Raman spectra obtained using the 1D Raman image, is up to four times higher than the Raman spectra measured without the imaging lens. The SNR for the 1D imaged spectra were 631, 683, 550, and 34 for the 942 cm<sup>-1</sup> 1043 cm<sup>-1</sup>, 1068 cm<sup>-1</sup>, and 1325 cm<sup>-1</sup> Raman bands of KClO<sub>4</sub>, NH<sub>4</sub>NO<sub>3</sub>, and the NaNO<sub>3</sub>/NaNO<sub>2</sub> mixture, respectively. Whereas, the SNR for the non-imaged spectra were 144, 474, 245, and 12 for the same

1D Raman images for some mineral samples are shown in Fig. 8, where the samples were vertically stacked (from upper to lower: quartz, gypsum, and calcite). The laser spot was 1.2 cm diameter at the sample. Fig. 8 shows the measured 1D Raman spectra using a cylindrical lens, a

photo of the sample, and the recorded images. The SNR improved up to 3 times in the imaged spectra compared to the collimated input spectra. The SNR for the calcite 1088 cm<sup>-1</sup> Raman band was 48 and 18, the 1010 cm<sup>-1</sup> gypsum Raman band was 89 and 82, and the 468 cm<sup>-1</sup> quartz Raman band was 168 and 113 in the imaged spectra and the non-imaged spectra, respectively. Note: a layer of anodized Al foil was placed between the rock layers to prevent Raman photon migration from sample-to-sample to simplify locating the row boundary in the image for each sample for data processing.

1D Raman measurements made using the monolithic SHRS gave similar results. Fig. 9 (left) shows the normal, non-imaged fringe image (FI, b) and the spatially resolved 1D Raman fringe image (FI, a, that incorporates a cylindrical imaging lens), for the sodium sulfate and sodium nitrate samples shown in the picture inset (upper left). The laser was focused so the 3 mm laser spot overlapped both cuvettes. A row by row FFT was used to obtain Raman spectra from each fringe image. The Raman spectrum in Fig. 9c results from the non-imaged fringe image (FI, b). As expected, the spectrum shows the combined signal of both components, showing both the sulfate and the nitrate bands. Spatially resolved spectra (Fig. 9a, b), from the 1D spatially resolved fringe image, were calculated from two spatially separated interferograms, each corresponding to parts of the 1D fringe image that overlap both cuvettes. The spatially resolved spectra, from the 1D images, show clear separation of the components in the two cuvettes. There is a small amount of overlap between the samples, possibly from diffuse light scatter and reflection from one region to another. The signal to noise ratio (SNR) for the Raman spectra collected via 1D imaging (9 a,b) was higher than the spectra without imaging (9c), 288 and 120 for sodium nitrate and sodium sulfate respectively in the 1D spectra, versus 85 and 59 for the unresolved spectra. The increased SNR in the 1D resolved spectra is the result of reduced shot noise in each spectrum. In the mSHS, like any interferometer, shot noise is equally distributed throughout all parts of the spectrum, so noise from strong bands reduces the SNR of weaker bands. This is what is shown in spectrum 9c. However, in the spatially resolved spectra, from the 1D images, shot noise from one component does not contribute to noise in the other component.

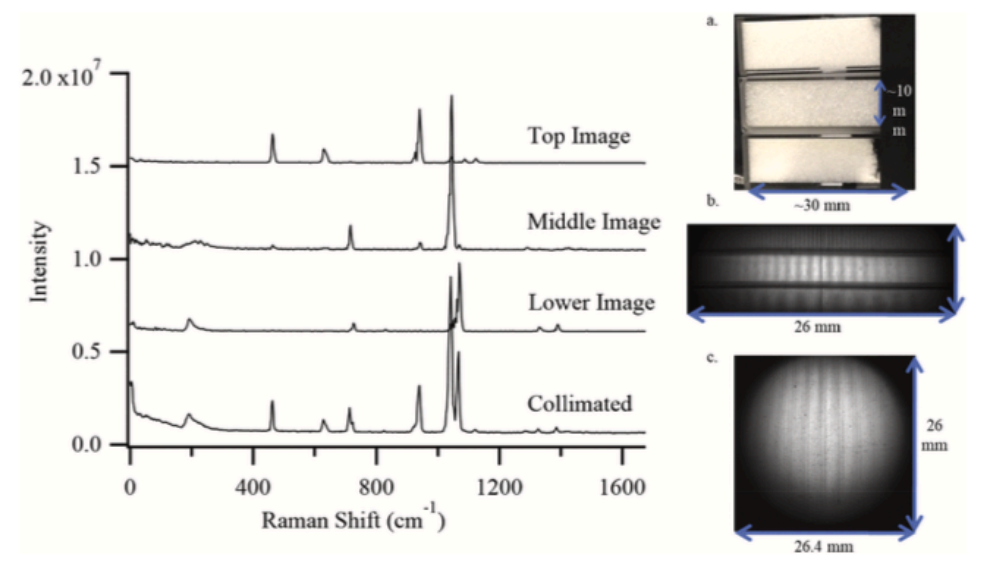


Fig. 7. Remote 1D Raman fringe image (b.) of the three samples shown in a., acquired using the benchtop SHRS with a cylindrical imaging lens, compared to fringe image acquired without using the cylindrical lens for imaging (c.). The samples (a.) consisted of three vertically stacked 1 cm cuvettes containing KClO<sub>4</sub>, NH<sub>4</sub>NO<sub>3</sub>, and a NaNO<sub>3</sub>/NaNO<sub>2</sub>. The Raman spectra labels indicate three distinct sample areas visible in the CCD 1D fringe image (b.). The Raman spectrum labeled Collimated corresponds to the CCD image on the right (c.), which contains no spatial information of the sample, measured without the cylindrical lens. All measurements made using ~1.15 W at 532 nm laser power, illuminating the sample with a 3.5-4 cm laser spot, using a 60 s acquisition. Spectra offset for clarity.

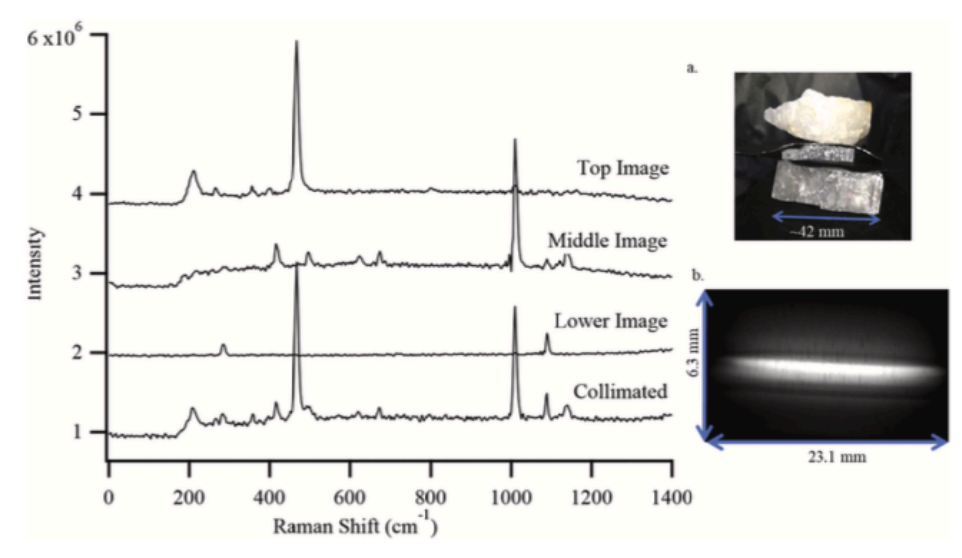


Fig. 8. Remote 1D Raman fringe image (b.) of the three samples shown in a., acquired using the benchtop SHRS with a cylindrical imaging lens. The sample consisted of a-quartz, gypsum, and calcite vertically stacked (a.). The Raman spectra labels indicate three distinct sample areas visible in the CCD 1D fringe image (b.). The Raman spectrum labeled Collimated corresponds to the non-imaged measurement made without the cylindrical lens. All spectra were measured using -1.15 W, 532 nm laser power, illuminating the sample with a -1.2 cm beam diameter with a 60 s acquisition. Spectra offset for clarity.

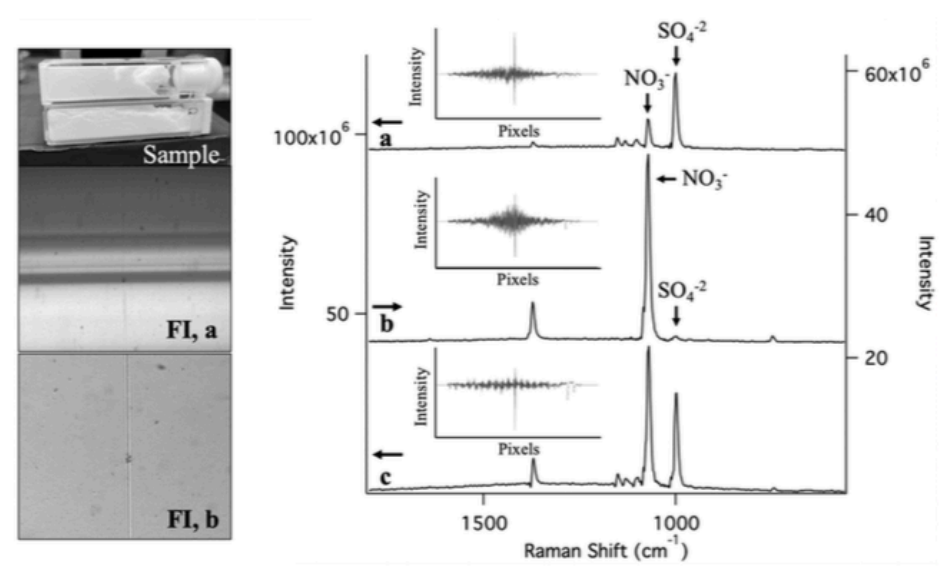


Fig. 9. 1D Raman fringe image (FI, a) of the three samples shown in the Sample picture, acquired using the monolithic SHRS with a cylindrical imaging lens, compared to fringe image acquired without the cylindrical lens for imaging (FI, b). The sample consisted of two vertically stacked 1 cm cuvettes containing Na<sub>2</sub>SO<sub>4</sub> and NaNO<sub>3</sub>. The corresponding Raman spectra are shown, where (a) and (b) are obtained from the 1D image using the cylindrical lens and (c) is obtained using the non-imaged fringe image, measured without the cylindrical imaging lens. The inserts show the interferograms/cross sections for each spectrum. Raman spectra were measured using ~165 mW, 532 nm laser power, illuminating the sample with a 3 mm beam diameter with a 300 s acquisition. Spectra offset for clarity.

## 4. Conclusion

Three spatial heterodyne Raman spectrometers, one benchtop and the others monolithic, have been used for remote Raman, LIBS, and 1D Raman imaging, for samples at a distance of 4.5 m. The wide area measurement capability of the SHS was demonstrated up to 60 mm for Raman and LIBS, and was shown to be useful to reduce sample photo-degradation in the case of Raman, using large laser spots on the sample, without loss of signal or decreased spectral resolution. 1D Raman imaging using a free standing SHRS and a monolithic SHRS was

demonstrated to provide better signal-to-noise ratio spectra for heterogenous samples than spectra measured without imaging. Improved SNR using 1D imaging is the result of spatial separation of the signal from different areas of the sample, which reduces the contribution of shot noise from stronger scattering samples from more weakly scattering adjacent samples.

#### Declaration of Competing Interest

The authors report there are no conflicts of interest.

#### Acknowledgments

We would like to thank the National Science Foundation [grant numbers CHE-1308211, OCE-1829327 and OCE-1829333] and NASA [grant numbers NNX14AI34G and 80NSSC19K1024] for funding this work.

#### References

- [1] C.M. Davies, H.H. Telle, D.J. Montgomery, R.E. Corbett, Quantitative analysis remote laser-induced breakdown spectroscopy (LIBS), Spectrochim. Acta Part B 50 (9) (1995) 1059-1075.
- S. Palanco, C. López-Moreno, J.J. Laserna, Design, construction and assessment of a [2] field-deployable laser-induced breakdown spectrometer for remote elemental sensing, Spectrochim. Acta Part B 61 (1) (2006) 88–95.
- [3] C. López-Moreno, S. Palanco, J.J. Laserna, F. Delucia Jr., A.W. Miziolek, J. Rose, R. A. Walters, A.I. Whitehouse, Test of a stand-off laser-induced-breakdown ectroscopy sensor for the detection of explosive residues on solid surfaces. Anal. At. Spectrom. 21 (2006) 55-60.
- [4] R. González, P. Lucena, L.M. Tobaria, J.J. Laserna, Standoff LIBS detection of explosive residues behind a barrier, J. Anal. At. Spectrom. 24 (8) (2009) 1123-1126.
- S.K. Sharma, A.K. Misra, P.G. Lucey, R.C.F. Lentz, A combined remote Raman and LIBS instrument for characterizing minerals with 532 nm laser excitation, Spectrochim. Acta A 73 (2009) 468-476.
- Cooney, Satellite observations using raman component of laser backscatter, in: R. Zirkind (Ed.), Proceedings of the Symposium of Electromagnetic Sensing of the Earth from Satellites, Polytechnic Institute of Brooklyn Press, New York, NY, 1967,
- [7] D.A. Leonard, Observation of Raman scattering from the att nitrogen ultraviolet laser, Nature. 216 (5111) (1967) 142–143.

  [8] T. Hirschfeld, Range independence of signal in variable focus remote raman
- spectrometry, Appl. Opt. 13 (6) (1974) 1435–1437.

  [9] R.M. Measures, Laser Remote Sensing: Fundamentals and Applications, John Wiley k Sons, New York, USA, 1984,
- [10] S.M. Angel, T.J. Kulp, T.M. Vess, Remote-raman spectroscopy at inter
- ranges using low-power CW lasers, Appl. Spectrosc. 46 (7) (1992) 1085–1091.

  [11] R.L. Aggarwal, L.W. Farrar, D.L. Polla, Measurement of the absolute raman cattering cross sections of sulfur and the remote raman detection of a 6 mm thick
- Sulfur Specimen at 1500 m, J. Raman Spectrosc. 42 (3) (2011) 461–464.
  S.K. Sharma, A.K. Misra, P.G. Lucey, R.C. Wiens, S.M. Clegg, Combined remote LIBS and Raman spectroscopy at 8.6 m of sulfur-containing minerals, and minerals coated with hematite or covered with basaltic dust, Spectrochim. Acta A 68 (4) (2007) 1036-1045.
- [13] J. Moros, J. J. Laserna. "New Raman-laser-induced breakdown spectroscopy identity of explosives using parametric data fusion on an integrated sensing platform". Anal. Chem. 83(16): 6275-6285.
- R. Grönlund, M. Lundqvist, S. Svanberg, Remote imaging laser-induced breakdown spectroscopy and remote cultural heritage ablative cleaning, Opt. Lett. 30 (21) (2005) 2882-2884
- [15] J. Moros, J.A. Lorenzo, P. Lucena, spectroscopy-laser-induced breaks \$0584-8547(21)00053-7/rf0065 is of explosives using a Mobile integra 39-1400.
- [16] NASA, SuperCam, htt am/ [accessed Feb 28 2020].
- [17] N.R. Gomer, C.M. Gordon, P. Lucey, S.K. Sharma, J.C. Carter, S.M. Angel, Rams spectroscopy using a spatial heterodyne spectrometer: proof of concept, Appl. Spectrosc. 65 (8) (2011) 849-857.

  [18] N. Lamsal, S.M. Angel, Deep-ultraviolet Raman measurements using a spatial
- heterodyne raman spectrometer (SHRS), Appl. Spectrosc. 69 (5) (2015) 525–534.

  [19] N. Lamsal, S.M. Angel, S.K. Sharma, T.E. Acosta, Visible and UV remote Raman neasurements in ambient light conditions using a gated spatial heterodyne ran ctrometer, Abstract 1459, 46th LPSC 2015. Woodland TX; March 16-20, 2015.
- [20] N. Lamsal, S.K. Sharma, T.E. Acosta, S.M. Angel, Ultraviolet stand-off Raman easurements using a gated spatial heterodyne raman spectrometer, Appl. Spectrosc. 70 (4) (2016) 666-685.

- [21] I.B. Gornushkin, B.W. Smith, U. Panne, N. Omenetto, Laser-induced breakdown d with spatial heterodyne spectroscopy, Appl. Spectrosc. 68 (9) (2014) 1076-1084
- [22] P.D. Barnett, N. Lamsal, S.M. Angel, Standoff laser-induced bre spectroscopy (LIBS) Using a miniature wide field of view spatial heterodyn eter with sub-microsteradian collection optics, Appl. Spectrosc. 71 (4) (2017) 585-590,
- range, K.C. Paul, S.M. Angel, Tran spatial heterodyne raman spectrometer (SHRS), Appl. Spectrosc. 71 (2) (2017)
- [24] A. Waldron, A. Allen, A. Colón, J.C. Carter, S.M. Angel, A monolithic spatial heterodyne Raman spectrometer: initial tests, Appl. Spectrosc. (2020), https://doi.org/10.1177/0003702820936643.
- [25] P. Barnett, S.M. Angel, Miniature spatial heterodyne Raman spectrometer with a cell phone camera detector, Appl. Spectrosc. 71 (5) (2016) 988–995.
- [26] A.N. Allen, S.M. Angel, Miniature spatial heterodyne spectrometer for laser induced breakdown spectroscopy and raman spectroscopy using fresnel collection. otics, Spectrochim, Acta B 149 (2018) 91-98
- [27] A.N. Allen, A.M. Waldron, J.M. Ottaway, J.C. Carter, S.M. Angel, Hyperspectral
- Raman imaging using a spatial heterodyne Raman spectrometer with a microlens Array, Appl. Spectrosc. (2020), https://doi.org/10.1177/0003702820906222.

  [28] P.D. Barrett, K.A. Strange, S.M. Angel, Improving spectral results using row-by-row fourier transform of spatial heterodyne raman spectrometer interferogram, Appl. Spectrosc. 71 (6) (2017) 1380-1386.
- [29] J.M. Ottaway, A.N. Allen, A.M. Waldron, P.H. Paul, S.M. Angel, J.C. Carter, Spatial heterody ne Raman spectrometer (SHRS) for in situ chemical sensing using sap
- and silica optical fiber raman probes, Appl. Spectrosc. 73 (10) (2019) 1160–1171.

  [30] J.M. Harlander, Spatial Heterodyne Spectroscopy: Interferometric Performance at any Wavelength without Scanning. [Ph. D. Dissertation], University of Wisconsin -Madison, Madison, Wisconsin, 1991.
- [31] J.M. Harlander, F.L. Roesler, R.J. Reynolds, K. Jaehnig, W.A. Sanders, Differential, field-widened spatial heterodyne spectrometer for investigations at high spectral resolution of the diffuse far ultraviolet 1548 Å emission line from the interstellar dium, Proc. SPIE 2006 (1993) 139-148.
- [32] J.M. Harlander, F.L. Roesler, S. Chakrabarti, Spatial heterodyne spectr novel interferometric technique for the FUV, Proc. SPIE 1344 (1990) 120–131.
- [33] J. Liu Bayanheshig, X. Qi, S. Zhang, C. Sun, J. Zhu, J. Cui, X. Li, Backscattering Raman spectroscopy using multi-grating spatial heterodyne rai Appl. Opt. 57 (33) (2018) 9735–9745.
- Qiu, X. Qi, X. Li, W. Xu, M. Zhao, Y. Tang, Y. Cheng, W. Li, Bayineshig Jirigalantu, Raman measurements using a field - widened spatial
- heterodyne raman spectrometer, J. Raman Spectrosc. 50 (2019) 1602–1613.

  [35] M.J. Egan, S.M. Angel, S.K. Sharma, Standoff spatial heterodyne Raman meter for mineralogical analysis, J. Raman Spectrosc. 48 (2017)
- [36] M.J. Egan, S.M. Angel, S.K. Sharma, Optimizing data reduction procedures in spatial heterodyne Raman spectroscopy with applications to planetary surface
- analogs, Appl. Spectrosc. 72 (6) (2018) 933–942.
  [37] G. Hu, W. Xiong, H. Shi, Z. Li, J. Shen, X. Fang, Raman spectroscopy detection for liquid and solid targets using a spatial heterodyne spectrometer, J. Raman ectrosc. 47 (2016) 289-298.
- [38] J. Qui, X. Qi, X. Li, Y. Tang, J. Lantu, X. Mi, H. Bavan, Broadband transmission ents using a field widened spatial hetero spectrometer with mosaic grating structure, Opt. Express 26 (20) (2018)
- [39] G. Hu, W. Xiong, H. Luo, H. Shi, Z. Li, J. Shen, X. Fang, B. Xu, J. Zhang, Ram spectroscopic detection for simulants of chemical warfare agents using a spatial heterodyne spectrometer, Appl. Spectrosc. 72 (1) (2018) 151–158.

  [40] G. Hu, W. Xiong, H. Luo, H. Shi, Z. Li, J. Shen, X. Fang, B. Xu, Spectral restoration method for spatial heterodyne Raman spectrometer, J. Raman Spectrosc. 48 (2017)
- 1633-1643.
- [41] S.M. Angel, N.R. Gomer, S.K. Sharma, C. McKay, Remote Ram planetary exploration: a review, Appl. Spectrosc. 66 (2) (2012) 137–150.

  [42] M. Prencipe, F. Pascale, C.M. Zicovich-Wilson, V.R. Sanders, R. Orlando, R. Dovesi,
- The vibrational spectrum of calcite (CaCO<sub>3</sub>): an ab initio quantum-mechanical lation, Phys. Chem. Miner. 31 (8) (2004) 559-564.
- [43] J.F. Scott, S.P.S. Porto, Longitudinal and transverse optical lattice vibrations in rtz, Phys. Rev. 161 (3) (1967) 903-910.
- [44] A. Chopelas, Single crystal raman spectra of forsterite, favalite, and monticellite, Am. Mineral, 76 (7–8) (191) 1101–1109.

  [45] C.P. Marshall, A.O. Marshall, Challenges analyzing gypsum on mars by Raman
- spectroscopy, Astrobiology 15 (9) (2015) 761–769.

  [46] D. Oelkrug, M. Brun, P. Hubner, K. Rebner, B. Boldrini, R.W. Kessler, Penetration of light into multiple scattering media: model calculations and reflectance experiments. Part II: the radial transfer, Appl. Spectrosc. 66 (8) (2012) 934–943.
- [47] D. Oelkrug, E. Ostertag, R.W. Kessler, Quantitative Raman spectrosco sion mode? Anal. Bioanal. Chem. 405 (10) (2013) natter: reflection or trans 3367-3379.
- [48] F. Hanke, U. Bottger, S.G. Pavlov, H.-W. Hubers, Raman spectra of fro olutions relevant for planetary surfaces, EPSC Abstracts. 9 (EPSC2014) (2014),
- [49] A. Kramida, Y. Ralchenko, J. Reader, NIST ASD Team, "NIST Atomic Spectra Database (version 5.3)." National Institute of Standards and Technol Gaithersburg, MD. http://physics.nist.gov/asd [accessed July 30 2020].

- [50] A. Wang, R.L. Korotev, B.L. Jolliff, Z. Ling, Raman imaging of extraterrestrial materials, Planet. Space Sci. 112 (July 2015) (2015) 23–34.
   [51] B.W. Smith, J.M. Harlander, Imaging spatial heterodyne spectroscopy: theory and practice, Proc. SPIE 3698 (1999) 925–930.
- [52] M.J. Egan, A. Colón, S. Michael Angel, Shiv Shama, Suppressing the multiplex disadvantage in photon-noise-limited interferometry using cross-dispersed spatial heterodyne spectrometry, 2020, https://doi.org/10.1177/0003702820946739. EXPRESS article.